ACS APPLIED MATERIALS & INTERFACES

Research Article

www.acsami.org

Ice Shear Fracture on Nanowires with Different Wetting States

Yang He,[†] Chengyu Jiang,*[,†] Shengkun Wang,[†] Yongcun Hao,[†] Jin Xie,[†] Xiaobao Cao,[†] Wei Tian,[‡] and Weizheng Yuan*[,†]

[†]Key Laboratory of Micro/Nano Systems for Aerospace, Ministry of Education and Shaan'xi Key provincial Laboratory of Micro and Nano Electromechanical Systems, School of Mechanical Engineering, and [‡]Key Laboratory of Space Applied Physics and Chemistry, Ministry of Education and Shaan'xi Key Laboratory of Macromolecular Science and Technology, School of Science, Northwestern Polytechnical University, Xi'an 710072, P. R. China

Supporting Information

ABSTRACT: Understanding the function of nanoscale structure morphology in ice adhesion properties is important in deicing applications. The correlation between ice adhesion and nanowire morphology as well as the corresponding ice shear fracture mechanism are presented for the first time. Ice adhesion on nanowires was measured using a tangential ice-detaching instrument that was developed in-house. Stress analysis was performed using a COMSOL software. Nanowire surface shifted from Wenzel to Cassie transition and Cassie wetting states when the nanowire length was increased. Tangential ice-detaching forces were greater on the hydrophilic surface than those on the hydrophobic surface. Ice−ice internal shear fracture occurred on the ice and force probe contact area at the Wenzel state or on the ice and nanowire contact area at Cassie transition and Cassie state. Different lengths of nanowires caused different wetting states; thus, different fracture areas were formed, which resulted in different tangential ice-detaching forces. This paper presents a new way of tailoring surface ice adhesion via rational design of nanowire morphology with different wetting states.

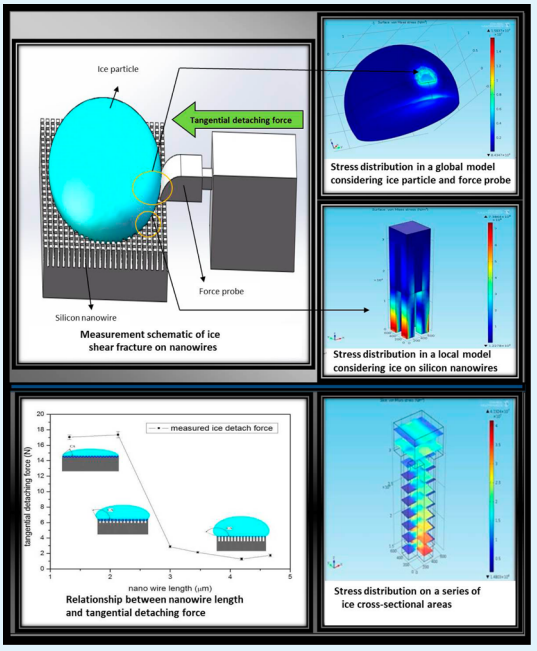

KEYWORDS: *ice adhesion, nanowire, shear fracture, morphology, wetting state, stress analysis*

1. INTRODUCTION

Surface icing can cause severe accidents and great economic losses in aircrafts, power lines, roads, ships, wind turbines, oil platforms, and telecommunication systems.[1,2] Current strategies for combating icing occurrence are generally resource-intensive and often have detrimental environmental consequences. A more appealing and universal strategy is to engineer surfaces that minimize both ice formation and adhesion. Scientists have explored the capability of superhydrophobic surfaces to mitigate icing problems.[3−22] Reducing ice adhesion by using superhydrophobic surfaces is of particular interest to the scientific community.[23−26] When ice adhesion is reduced, ice may be easily cleared by human assistance or natural forces such as wind, gravity, and vibration. A common theme in ice adhesion research is the comparison of ice adhesion strength and water wettability. A high contact angle causes low adhesion force.[27] Correlation exists between wetting hysteresis and ice adhesion strength on rough surfaces with similar chemistry components.[28,29] A linear relationship between ice adhesion strength and water wettability parameter $1+\cos\theta_{Rec}$ (where θ_{Rec} is the receding contact angle of water) has been reported.[30] However, the relationship of ice adhesion and wettability is not enough to fully understand the mechanism of ice adhesion. Cao et al.[3] argued that determining if a superhydrophobic surface is anti-icing is difficult without a detailed knowledge of surface morphology. Meuler et al.[30] suggested that further reduction in ice adhesion strength requires textured surfaces. Meuler, McKinley, and Cohen[31] pointed out the need to explore how topographical texture impacts ice-phobicity. Several researchers have explored the effect of texture topography on ice adhesion. Several of them reported that rough surfaces lead to high ice adhesion strength.[32,33] Others found that micro-nano dual structures dramatically reduce ice adhesion.[34−36] Nevertheless, the

Received: July 25, 2014
Accepted: September 19, 2014
Published: September 19, 2014

correlation between nano structure (typically nanowires) morphology and ice adhesion has not been reported, and the mechanism of ice fracture on microscale structures remains unclear.

This study aimed to identify the correlation between ice adhesion and nanowire morphology as well as the corresponding ice shear fracture mechanism. Ice adhesion on nanowires was measured using a tangential ice-detaching instrument that was developed in-house. Stress analysis was performed using a COMSOL software. The relationship between nanowire morphology and ice-detaching force and wettability was investigated. A thorough discussion on the mechanism of how ice detaches from a nanowire surface with different wettabilities is presented. This study is necessary to understand the function of nanoscale structure morphology in anti-icing/ice-phobic properties. The study offers a new way to tailor surface ice adhesion via nanowire morphology.

2. EXPERIMENT

Materials. The substrates used were (100)-oriented p-type silicon wafers with a thickness of 500 μm (Shanghai Jun He Corp.). Acetone (w% $\geq$ 99.5, Lian Longbowa Chemicals Corp., Tianjin, China) and ethanol (w% $\geq$ 99.7, Lian Longbowa Chemicals Corp., Tianjin, China) were used in the precleaning process. Deionized water from water purification system in the lab (>15MΩ-cm, Chinese Electrical Design Institution) and N_2 (AR, 99.999%, Tiansheng Industrial Gas Corp., Xixiang, China) were used in the pre- and postcleaning process. HF (w % $\geq$ 40, Longxi Chemicals Corp., Sichuan, China), $AgNO_3$ (AR, Hongyan Chemicals Corp., Tianjin, China), and $Fe(NO_3)_3$ (AR, Aojia Chemicals Corp., Nanjing, China) were used in the galvanic etching process.

Nanowire Fabrication. Silicon wafers were cleaned with acetone (5 min), ethanol (5 min), and deionized water (2−3 times). They were then thoroughly rinsed with a mixed solution of HF (4.6 mol/L)/$AgNO_3$ (0.01 mol/L) for 1 min. They were further immersed in a mixed solution of HF (4.6 mol/L)/ $Fe(NO_3)_3$ (0.05 mol/L) at 30 °C for 10, 20, 30, 40, 50, and 60 min. Finally, they were rinsed with deionized water and dried by N_2 flow at room temperature. A series of nanowires with different morphologies was obtained. The fabrication details were presented in a previous study.[37]

Surface Characterization. The silicon surface morphology was observed using a scanning electron microscope (SEM, JEOL, JSM-6309A). The apparent contact angles (CA) and contact angle hysteresis (CAH) of the as-prepared silicon nanowire surfaces were measured using an optical goniometer (OCA15EC, Data Physics Company Ltd.). Deionized water droplets with a volume of 10 μL were used in CA measurements. CAH was calculated by subtracting the receding angle (θ_R) from the advancing angle (θ_A). Deionized water droplets with a volume of 10 μL and increments of 1 μL were used in the advancing and receding angle measurements. The experiments were performed at 20 °C and 15% relative humidity.

Ice Shear Fracture Measurement. The measurement schematic of ice shear fracture on nanowires is shown in Figure 1. Although goniometers are widely used to measure liquid contact angles, no analogous instruments are available to measure ice shear fracture strength. To solve this problem, we designed an ice adhesion test instrument to measure the shear force required to tangentially remove ice from a test surface, as shown in Figure 2. A sample substrate was clamped on a base plate (top), and 10 μL of deionized water was deposited on the base plate surface by using a pipet. It was then placed in a cryogenic box at −15 °C for 1−2 min. Ice particles were removed from the test substrate by propelling the probe of a force transducer (SUNDOO, SH-50) with a speed of 0.5 mm/s that was driven by a step motor. The probe was moved 0.4 mm above the surface to avoid touching the substrate. The maximum force at break was recorded as the tangential ice-detaching force. The experimental details were presented in a previous study.[36]

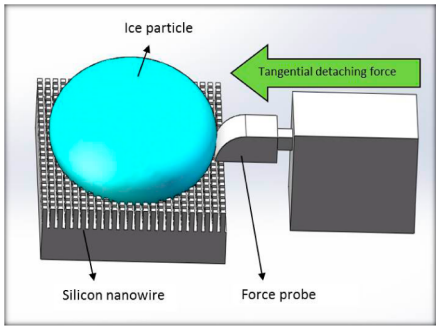

Figure 1. Measurement schematic of ice shear fracture on nanowires.

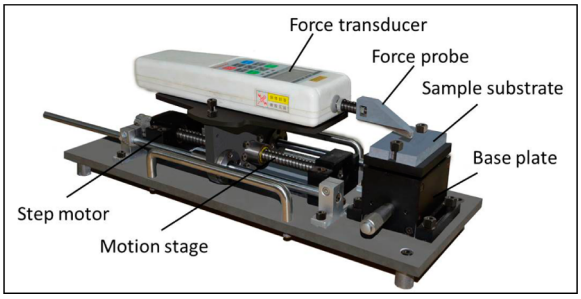

Figure 2. Tangential ice-detaching measuring instrument that was developed in-house.

3. RESULTS AND DISCUSSION

Silicon nanowires with various morphologies were obtained via the galvanic etching method. The SEM images of the nanowires with different etching times are shown in Figure 3. The nanowire length increased from 1.32 to 4.67 μm when the etching time was increased from 10 to 60 min, while the nanowire width was ∼200 nm in most cases. The average length of the nanowires, CAs, CAHs, and tangential detaching forces (−15 °C, 0.5 mm/s probe velocity) are presented in Table 1. The mean values were calculated from three individual measurements. Uncertainties were obtained from the standard deviation of the measurements.

The relationship of nanowire length and tangential detaching force is shown in Figure 4. The tangential detaching force slightly changed when the nanowire length was less than the threshold value. The relative error was small ($\varepsilon_{relative}$ = (17.36 N − 17.04 N)/17.36 N = 1.8%). Only when the nanowire length was greater than the threshold value did the tangential detaching force dramatically change from 17.36 to 2.88 N, which decreased by more than six times. When the nanowire length was further increased, the tangential detaching forces slightly decreased (from 2.88 to 1.28 N). In this study, the threshold value was between 2.13 and 3.46 μm.

Further investigating the correlation between nanowire morphology and wettability is necessary because previous studies have shown that wettability influenced ice adhesion. The relationship of nanowire length and CA and CAH is shown in Figure 5. When the nanowire length was less than 2.13 μm, the surface was hydrophilic with small CAs (17°/37.9°) and large CAHs (9.5°/6.7°). When the nanowire length increased to 3 μm, the surface became hydrophobic with a large CA (109.7°) and small CAH (3.2°). When the nanowire length was further increased from 3.46 to 4.67 μm, the surface was close to superhydrophobic with larger CAs (140.9°/149.8°/142.2°) and smaller CAHs (0.5°/0.3°/2.4°). In general, increasing CAs and

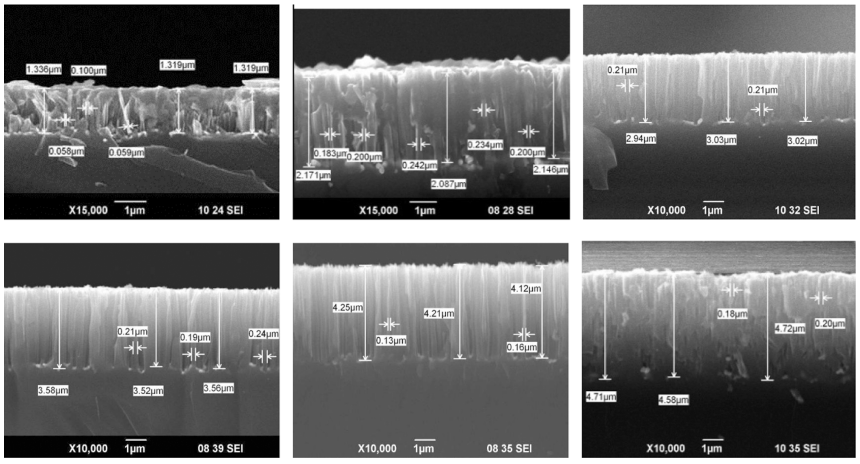

Figure 3. SEM images of the nanowires produced at different etching times from 10 to 60 min at increments of 10 min.

Table 1. Measurement Results of Nanowire Morphology, Wettability, And Tangential Detaching Force

no.	etching time (min)	nanowire length, h (μm)	CA (deg)	CAH (deg)	tangential detaching force, F (N)
1	10	1.32 ± 0.01	17.0 ± 4.1	9.5 ± 3.1	17.04 ± 0.31
2	20	2.13 ± 0.04	37.9 ± 5.2	6.7 ± 2.3	17.36 ± 0.39
3	30	3.00 ± 0.06	109.7 ± 3.6	3.2 ± 2.1	2.88 ± 0.15
4	40	3.46 ± 0.19	140.9 ± 2.5	2.5 ± 0.4	2.13 ± 0.08
5	50	4.19 ± 0.07	149.8 ± 1.0	0.3 ± 0.1	1.28 ± 0.15
6	60	4.67 ± 0.08	142.2 ± 1.8	2.4 ± 0.5	1.75 ± 0.17

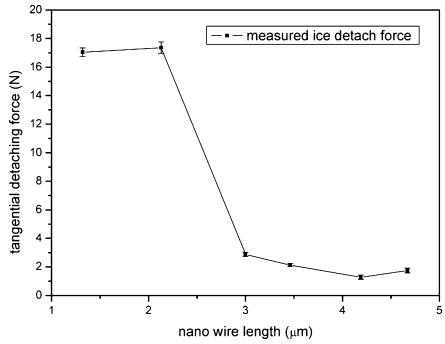

Figure 4. Relationship between nanowire length and tangential detaching force.

decreasing CAHs were observed as the nanowire length was increased.

The results indicated that nanowire morphology exhibited great influence on wettability and ice adhesion. The surface shifted from hydrophilic to hydrophobic when the nanowire length was increased greater than the threshold value. Tangential ice-detaching forces were greater on the hydrophilic surface than those on the hydrophobic surface. The detaching force did not significantly change on the hydrophilic surface, whereas on the hydrophobic surface, forces decreased when the CAs increased and the CAHs decreased.

Corresponding mechanisms were further investigated to determine how nanowire morphology influences wettability, how ice detaches from a nanowire surface with different wettability, and why forces in different nanowire morphologies differ.

The relationship between nanowire length and wettability was explained by different wetting states,[38−40] as shown in Figure 6. When the nanowire length was less than the threshold value, water completely penetrated the groove, which demonstrated Wenzel wetting state and hydrophilic wettability, as shown in Figure 6a. When the nanowire length was increased, water partially penetrated the groove, which demonstrated Cassie transition wetting state[41−43] and hydrophobic wettability, as shown in Figure 6b. The partially

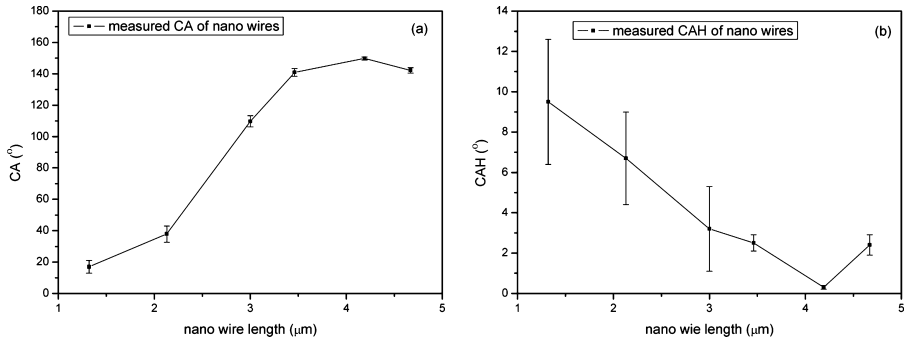

Figure 5. Relationship of nanowire length with (a) CA and (b) CAH.

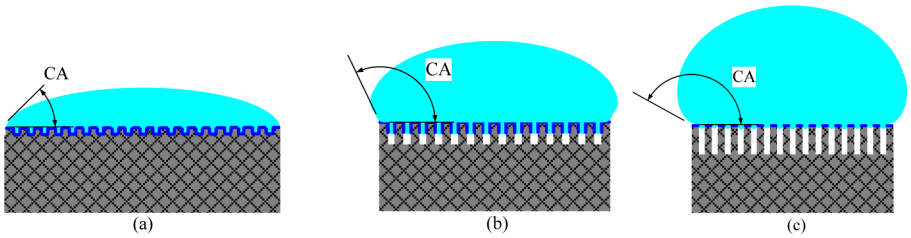

Figure 6. Different wetting states as a result of different nanowire lengths: (a) Wenzel wetting state, (b) Cassie transition wetting state, and (c) Cassie wetting state.

penetrated height of water, h_p, was calculated based on the Cassie–Baxter theory (h_p = 1.565 μm, this value was used in further stress analyses).[44] When the nanowire length was increased above the threshold value, water resided on top of the nanowires, which demonstrated Cassie wetting state and close to superhydrophobic wettability, as shown in Figure 6c.

The wetting state transition and nano roughness effect could be explained by energetic barrier theory.[45−47] If microstructures are built of a hydrophobic material, the energy barrier should be surmounted for wetting transition to proceed. This energy barrier corresponds to the surface energy variation between the Cassie state and the Cassie transition state. When water penetrates into micro structure, the solid–liquid interface grows while the air–liquid interface over micro structure is retained. Therefore, the interface free energy increases continuously and attains its maximal value when liquid wets the side surfaces almost completely. As for hydrophilic surfaces, the Cassie wetting state is possible due to the "geometrical air trapping effect"[48] although wetting is always energetically favorable. When water fills the hydrophilic slot, the energy gain due to the wetting of the hydrophilic wall is overcompensated by the energy increase at the expense of the growth of the high-energetic liquid–air interface. As to the reverse transition from the Wenzel state to the Cassie one, the energy barrier is much larger than for the direct transition, thus the reverse transition is irreversible.

In our experiments, the substrate is silicon which can be regarded as hydrophobic material (In microelectronic, silicon is often regard as hydrophobic material). The nanowire width was nearly unchanged ($w \approx 200$ nm) and the nanowire length increased (h increase from 1.32 to 4.67 μm). Thus, the energetic barrier separating the Cassie and Wenzel states can be calculated using eq 1[46]

$$W = 2\pi R^2 h(\gamma_{SL} - \gamma_{SA})/p = -2\pi R^2 h\gamma_{LA}\cos\theta_Y/p \quad (1)$$

where h denotes the nanowire length, p denotes the sum of nanowire width w and space s, R denotes the radius of the droplet contact area, θ_Y denotes Young contact angle or instinct contact angle of the surface, and γ_{SL}, γ_{SA}, and γ_{LA} denote the surface tensions at the solid–liquid, solid–air, and liquid–air interfaces, respectively. Equation 1 apparently showed that the energy barrier will monotonously increase when nanowire length increase and nano wire width and space keeps stable. It deduced that nanowires with greater length will have greater energetic barrier, making the Cassie state more stable. On the contrary, nanowires with less length will have less energetic barrier which could be surmounted more easily, making Cassie state transferred to Cassie transition state and even Wenzel state.

The ice-detaching process on the nanowire surface with different wetting states was also investigated. Ice detachment refers to the internal fracture of ice layer or external fracture of the ice–silicon interface. The question is how these fracture occurred. Unfortunately, observing the fracture process experimentally is difficult. An alternative strategy with the use of computational simulation was employed to analyze the fracture process. Computational stress analysis was performed using a COMSOL software.

Figure 7 shows the schematic of the geometric parameters employed for stress analysis. Ice was simplified as a segment

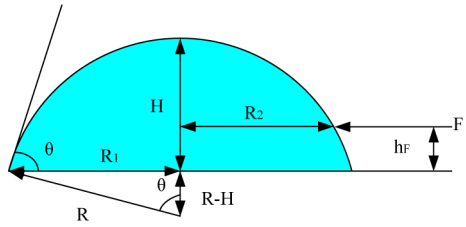

Figure 7. Schematic of the geometric parameters employed for stress analysis.

(part of a sphere), R denotes the radius of the segment, H denotes the distance from the summit of the segment to the surface, R_1 denotes the radius of the projection circle of the segment bottom on the surface, h_F denotes the distance from the external force F to the surface, R_2 denotes the radius of the cross-sectional circle located at distance h_F, and θ denotes the apparent contact angle (angle between the tangent line of the three-phase contact point on the segment profile and the surface).

In this experiment, ice particle volume V = 10 μL and θ were the CA values from Table 1. Thus, the corresponding geometric parameters were derived (details about calculation of the geometric parameters employed for stress analysis could be seen in the supporting materials). The model was simplified by setting the widths (w) and spaces (s) of the silicon nanowires at 200 nm because these parameters did not significantly vary in the experiments. The lengths (h) of the silicon nanowires were experimentally measured, as shown in Table 2. All of the geometric parameters employed for stress analysis are shown in Table 3.

Ice can be regarded as a linear elastic material at −3° to −40°, and brittle fracture occurs on ice when the strain rate > 1 × 10^{-3} s^{-1}.[49] In the present study, ice particles were detached with a displacement of 1 mm to 4 mm within 1 s. The strain rate was larger than 1 × 10^{-3} s^{-1}; thus, brittle internal fracture caused by shear stress was expected to occur. The ice–ice shear fracture strength ($\sigma_{shear-ice-ice}$) was set at 4 MPa based on a previous study.[49] Silicon fracture strength ($\sigma_{fracture-silicon}$) was set at 7000 MPa and iron fracture strength ($\sigma_{fracture-iron}$) was set at greater than 1000 MPa according to the internal material

Table 2. Geometric Parameters Employed for Stress Analysis

no.	w (nm)	s (nm)	h (nm)	R (mm)	H (mm)	R_1 (mm)	R_2 (mm)
1	200	200	1320	11.86	0.52	3.47	1.683
2	200	200	2130	4.24	0.9	2.61	1.997
3	200	200	3000	1.47	1.97	1.38	1.467
4	200	200	3460	1.37	2.42	0.84	1.206
5	200	200	4190	1.34	2.5	0.67	1.1014
6	200	200	4670	1.35	2.41	0.83	1.172

Table 3. Material Parameters Employed for Stress Analysis

item material	density (kg/m^3)	Young's modulus (GPa)	Poisson ratio	fracture stress (MPa)
ice	900	2.994	0.3	4 (shear fracture)
silicon (nanowire)	2329	170	0.28	7000
iron (force probe)	7850	200	0.33	>1000

parameters of COMSOL. The material parameters employed for stress analysis are listed in Table 3.

The analysis strategy we adopted is described as follows. First, we established a global model that considered ice particles and force probe to determine the position of the global maximum stress area. We then established a local model that considered ice on silicon nanowires to determine the position of the local maximum stress area. The maximum stress was obtained by comparing the simulation results from both the global and local models. The specific area where fracture occurred was located by comparing the maximum stress and the material fracture strength. Stress analyses were based on continuous mechanics because ice was regarded as an elastic material and its dimensions were not in molecular scale.

Figure 8 shows the stress analysis results of a global model at the Wenzel–Cassie transform state. Figure 8a shows a global model considering ice particle contact with force probe. The ice particle was simplified as a segment with geometric and material parameters (No. 3) in Tables 2 and 3. The force probe was simplified as an iron block contact with an ice segment. The boundary conditions included displacement and force conditions, which were coincident with the experiments. The displacement condition was set such that the bottom area of the ice segment was fixed, and the force condition was set such that an experimental force (2.88 N) was applied on the ice-probe contact area by an iron block. The models were meshed, and an appropriate numerical algorithm was adopted (nonlinear algorithm was chosen because it enabled simulation convergence). The iron force probe was rigid, and no fracture phenomenon was observed; thus, the stress on the iron force probe was not considered. The simulation result of stress distribution in a global model is shown in Figure 8b. The colored bar shows the magnitude of stress in which the blue bar denotes less stress and the red bar denotes greater stress. Maximum stress occurred on the ice–probe contact area or ice–silicon contact area. The enlarged images of stress distribution on the two areas were further observed to gather more details. Figure 8c shows the enlarged image of stress distribution on an ice–probe contact area. The maximum stress on this area occurred at the bottom, and the value of this stress ($\sigma_{max-probe}$) was =15.94 MPa. Figure 8d shows the enlarged image of stress distribution on an ice–silicon contact area. The maximum stress on this area occurred on the contact front area, and the value of the maximum stress ($\sigma_{max-silicon}$) was = 7.30

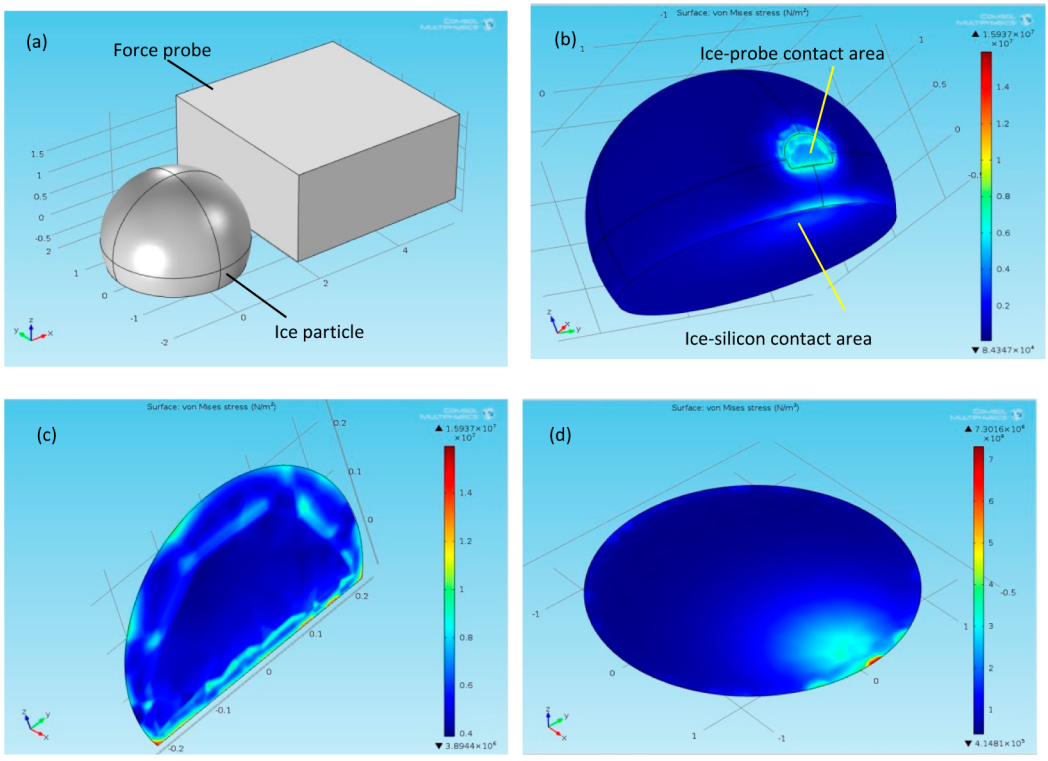

Figure 8. Stress analysis results of a global model at Cassie transition state: (a) global model considering ice particle contact with force probe, (b) stress distribution in a global model, (c) enlarged image of stress distribution on the ice–probe contact area, and (d) enlarged image of stress distribution on the ice–silicon contact area.

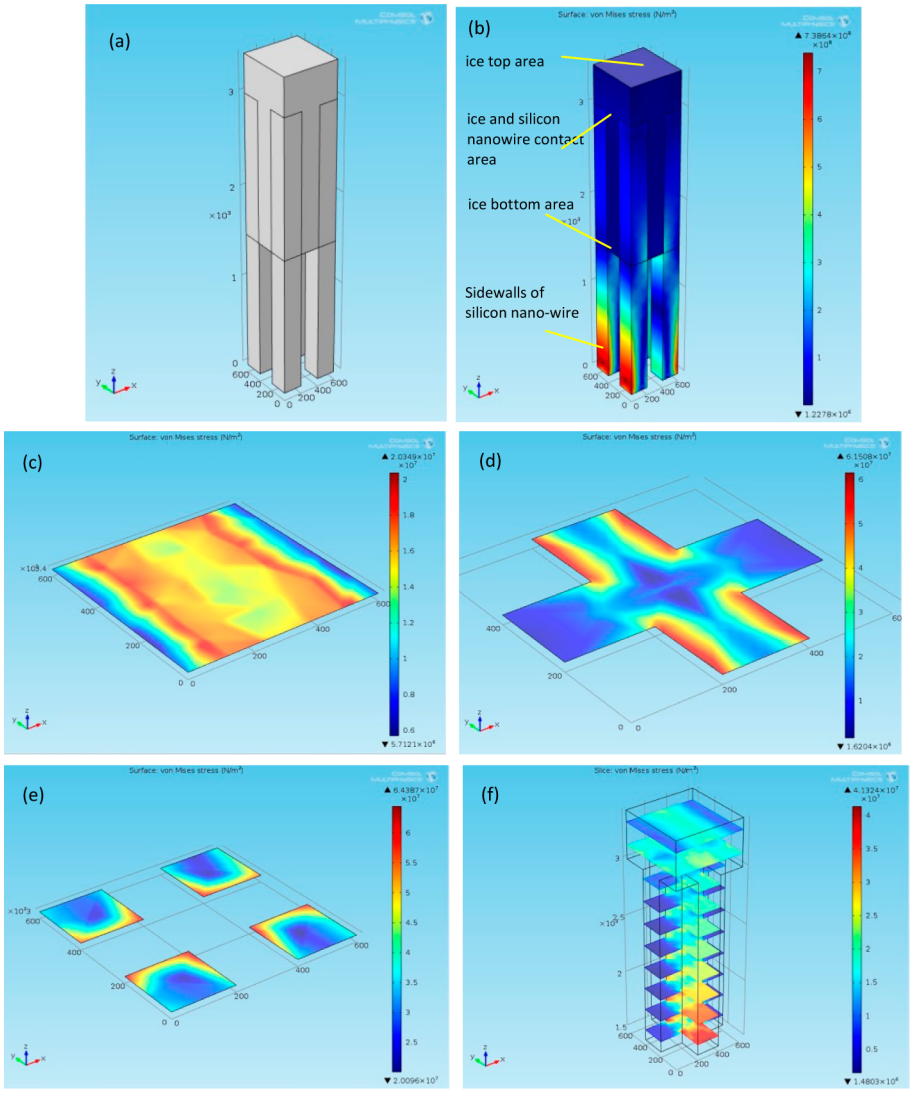

Figure 9. Stress analysis results of a local model at Cassie transition state: (a) local model considering ice on silicon nanowires, (b) stress distribution in a local model, (c) stress distribution on the top area of the ice, (d) stress distribution on the bottom area of the ice, (e) stress distribution on the ice and silicon nanowire contact area, and (f) stress distribution on a series of ice cross-sectional areas.

MPa. The stress on the ice−probe contact area was greater than that on the ice−silicon contact area, and both were greater than the ice−ice shear fracture strength ($\sigma_{shear-ice-ice}$ = 4 MPa). The ice appeared to be fractured on the ice−probe contact area. A conclusion based on these results is premature because the results were obtained on a macro scale level. Further investigating the maximum stress area on the ice−silicon contact area at a microscale level and drawing the right conclusion considering both macro- and microcale results are necessary.

The local maximum stress on a microscale level was further analyzed. Figure 9 shows the stress analysis results of a local model at Cassie transition state. Figure 9a shows a local model considering ice on the silicon nanowires. In the simplified unit, ice particles were described as a block embedded in four prismatic nanowires. The ice partially penetrated the silicon nanowires because the structure demonstrated the Cassie transition wetting state (penetrated height h_p = 1.565 μm). The boundary conditions were set as follows: the displacement of the silicon nanowire bottom was fixed and the value of unit force applied on the ice block top was equal to maximum stress on the ice−silicon contact area, which was obtained from the global model (7.30 MPa). Figure 9b shows the stress distribution in a local model. The maximum stress occurred near the bottom areas on the side walls of the silicon nanowires. The maximum stress ($\sigma_{max-silicon}$) was 738.64 MPa. However, this value was less than the silicon fracture stress ($\sigma_{max-silicon} < \sigma_{fracture-silicon}$ = 7000 MPa); thus, the silicon nanowires were not expected to fracture. The stress distribution on the different cross-sectional areas of ice was further analyzed to determine where the maximum ice−ice internal stress occurred. Figure 9c shows the stress distribution on the top area of the ice and the maximum stress on this area ($\sigma_{max-ice-top}$) was 20.35 MPa. Figure 9(d) shows the stress distribution on the bottom area of the ice, and the maximum stress on this area ($\sigma_{max-ice-bottom}$) was 61.51 MPa. Figure 9e shows the stress distribution on the ice and silicon nanowire contact area, and the maximum stress on this area ($\sigma_{max-ice-nanowire-contact}$) was 64.39 MPa. The stress distributions on a series of the ice's cross-sectional areas were analyzed to investigate the variation trend of stress distribution inside the ice, as shown in Figure 9f. The stress was greater when the cross-sectional area was closer to the ice and silicon

Table 4. Stress Analysis Results (MPa)

		global model		local model			
no.	wetting state	$\sigma_{max-probe}$	$\sigma_{max-silicon}$	$\sigma_{max-ice-top}$	$\sigma_{max-ice-bottom}$	$\sigma_{max-ice-nanowire-contact}$	$\sigma_{max-nanowire}$
1	Wenzel	689.82	13.80	36.30	11.56	162.96	665.56
2	Wenzel	845.45	18.53	47.70	19.4	179.71	1053.9
3	Cassie transition	15.94	7.30	20.35	61.51	64.39	738.64
4	Cassie	7.69	4.69	15.76	-	437.01	916.65
5	Cassie	1.90	5.76	22.70	-	622.15	1239.4
6	Cassie	2.10	4.02	16.51	-	536.18	950.31

nanowire contact area. The maximum stress in the local model occurred on the ice and silicon nanowire contact area ($\sigma_{max-ice-nanowire-contact} > \sigma_{max-ice-bottom} > \sigma_{max-ice-top}$). The simulation results from the global model (macroscale) and the local model (micro scale) were compared and the maximum stress occurred on the ice and silicon nanowire contact area ($\sigma_{max-ice-nanowire-contact} > \sigma_{max-probe}$).

Furthermore, the maximum stress was compared with the ice−silicon interface fracture strength and the ice−ice internal fracture strength to determine the kind of fracture that occurred. Unfortunately, no accurate report is available on the ice−silicon interface fracture strength. The ice−silicon interface fracture strength may come from a molecular interfacial force (7×10^2 MPa to 7×10^3 MPa) and a chemical bonding force (7×10^3 MPa to 7×10^4 MPa).[50] Apparently, the magnitude of maximum stress that was obtained from simulation was lesser than that of the combination of molecular interfacial and chemical bonding force ($\sigma_{max-ice-nanowire-contact} = 64.39$ MPa $< 7 \times 10^4$ MPa). The result suggests that the detachment of ice in the nanowires may not be caused by the ice−silicon interface fracture. However, the maximum stress was greater than the ice−ice shear fracture strength ($\sigma_{max-ice-nanowire-contact} = 64.39$ MPa $> \sigma_{shear-ice-ice} = 4$ MPa). The result suggests that the detachment of ice in the nanowires can be attributed to the ice−ice internal shear fracture. Thus, the ice shear fracture occurred on the ice and silicon nanowire contact area when the surface showed Cassie transition wetting state.

It is clearly seen from Figures 8 and 9 that the distribution of stresses is nonhomogeneous, and the stresses are maximal in the nearest vicinity of the triple line. This supports the idea that the Cassie−Wenzel transition is expected to start from the triple line. This theme was intensively debated in the literature; it was supposed that wetting transition start from the center of a droplet,[51] and in contras,t it was suggested that the Cassie−Wenzel transition starts from events occurring in the vicinity of the triple line.[52,53] It seems that the findings support the second scenario.

All of the parameters from Tables 2 and 3 were substituted into a corresponding simulation model. The stress analysis results are shown in Table 4. As for simulations 1 and 2, the Wenzel state models were used based on experiment results. The maximum stresses on the side walls of the silicon nanowires were lesser than the silicon fracture length ($\sigma_{max-silicon} = 665.56$ MPa/1053.9 MPa $< \sigma_{fracture-silicon} = 7000$ MPa); thus, the silicon nanowires were not expected to fracture. In the global model, the maximum stress appeared in the ice−probe contact areas ($\sigma_{max-probe} = 689.82$ MPa/845.45 MPa $> \sigma_{max-silicon} = 13.80$ MPa/18.53 MPa). In the local model, the maximum stress appeared in the ice and silicon nanowire contact areas ($\sigma_{max-ice-nanowire-contact} = 162.96$ MPa/179.71 MPa $> \sigma_{max-ice-top} = 36.3$ MPa/47.7 MPa $> \sigma_{max-ice-bottom} = 11.56$ MPa/19.4 MPa).

Comparison of the global and local model data showed that the stress on the ice−probe contact area was greater than the stress on any other contact zones, and it was greater than the ice−ice shear fracture strength ($\sigma_{max-probe} > \sigma_{max-ice-nanowire-contact} > \sigma_{shear-ice-ice}$). This result means that the stress on the ice−probe contact area largely increased within the same time and easily reached the value of the ice−ice shear fracture strength; thus, ice preferentially fractured on this area. In summary, the ice−ice shear fracture occurred on the ice−probe contact area at Wenzel state.

As for simulations 4, 5, and 6, the Cassie state models were used based on the experimental results. The silicon nanowires did not fracture ($\sigma_{max-silicon} = 916.65$ MPa/1239.4 MPa/950.31 MPa $< \sigma_{fracture-silicon} = 7000$ MPa). In the global model, the maximum stress appeared in the ice−probe contact area in No. 4 ($\sigma_{max-probe} = 7.69$ MPa $> \sigma_{max-silicon} = 4.69$ MPa), whereas the maximum stress appeared in the ice−silicon contact area in simulations 5 and 6 ($\sigma_{max-probe} = 1.90$ MPa/2.10 MPa $< \sigma_{max-silicon} = 5.76$ MPa/4.02 MPa). In the local model, the maximum stresses appeared in the ice and silicon nanowire contact areas ($\sigma_{max-ice-nanowire-contact} = 437.01$ MPa/622.15 MPa/536.18 MPa $> \sigma_{max-ice-top} = 15.76$ MPa/22.70 MPa/16.51 MPa). The stress on the ice and silicon nanowire contact areas was greater than that on any other contact zones and was greater than the ice−ice shear fracture strength ($\sigma_{max-ice-nanowire-contact} > \sigma_{max-probe} > \sigma_{shear-ice-ice}$). This result indicated that the ice shear fracture occurred on the ice and silicon nanowire contact area at the Cassie state.

There are some indirect evidence to support the computational conclusion. It is experimental observed that there is a thin layer of residual ice on the sample surface at Wenzel state, indicating that the ice−ice shear fracture occurred on the ice−probe contact area at Wenzel state. There is no obvious residual ice on the sample at Cassie state and Cassie transition state, indicating that the ice shear fracture occurred on the ice and silicon nanowire contact area at these two wetting state. We expect the direct evidence in the future if new technology is invented and ice shear process on nanowires could be observed directly.

The stress analysis results revealed the position and kind of ice fracture that occurred. Tangential detaching forces differed with different nanowire lengths, as discussed further. The tangential force F was equal to the multiplication of shear stress (σ) and fracture area (S) ($F = \sigma S$). The ice−ice shear fracture strength ($\sigma_{shear-ice-ice}$) was identical; thus, the difference came from the fracture area. At the Wenzel state, the fracture areas were cross-sectional areas located at ice−probe contact area. At the Cassie transition and Cassie state, the fracture areas were ice and silicon nanowire contact areas. The fracture area at the Wenzel and Cassie transition/Cassie states was calculated using

eqs 2 and 3. The parameters of theses equations are listed in Table 2.

$$S_{\text{fracture}-\text{Wenzel}} = \pi {R_2}^2 \quad (2)$$

$$S_{\text{fracture}-\text{transition}/\text{Cassie}} = \frac{S_{\text{solid}}}{S_{\text{solid}} + S_{\text{air}}} S_{\text{projection}} = \left(\frac{w_{\text{nano}}}{w_{\text{nano}} + s_{\text{nano}}}\right)^2 \pi {R_1}^2 \quad (3)$$

The calculated fracture areas are listed in Table 5. The relationship between fracture area and tangential detaching force is shown in Figure 10. The result showed that the fracture areas were greater at the Wenzel state than those at the Cassie transition and Cassie states; thus, tangential detaching forces at Wenzel state were correspondingly greater. The tangential detaching forces increased with increasing fracture area at the Cassie state. However, only a slight change in forces was observed at the Wenzel state even if the calculated fracture area obviously changed. The reason may be due to the spreading of water at the Wenzel state, thereby resulting in similar fracture areas. In summary, different nanowire lengths resulted in different wetting states, which resulted in different fracture areas and different tangential detaching forces.

Table 5. Calculated Fracture Area versus Experimental Tangential Detaching force

no.	wetting state	S_{fracture} (mm^2)	F (N)
1	Wenzel	8.90	17.04 ± 0.31
2	Wenzel	12.53	17.36 ± 0.39
3	Cassie transition	1.5	2.88 ± 0.15
4	Cassie	0.55	2.13 ± 0.08
5	Cassie	0.35	1.28 ± 0.15
6	Cassie	0.54	1.75 ± 0.17

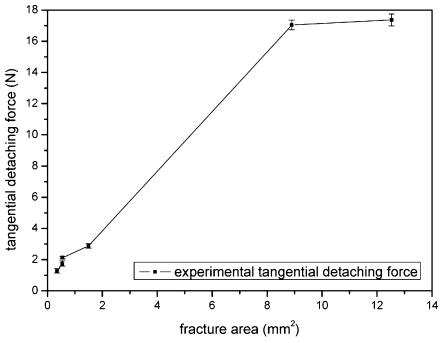

Figure 10. Relationship between fracture area and tangential detaching force.

CONCLUSION

This study interpreted the mechanism of ice shear fracture on nanowires with different wetting states via experiment and computational analyses. The results showed that the surface transferred from the Wenzel to the Cassie transition and Cassie wetting states when the nanowire length was increased. The tangential ice-detaching force was greater on the hydrophilic surface than that on the hydrophobic surface. Tangential ice-detaching forces were similar at the Wenzel state, but they decreased when CA increased and CAH decreased at the Cassie state. Ice shear fracture occurred on the ice and force-probe contact area at the Wenzel state or on the ice and silicon nanowire contact area at the Cassie transition and Cassie states. The different length of nanowires led to different wetting states and fracture areas, thereby resulting in different tangential detaching ice forces. On the basis of these results, ice adhesion can be tailored via rational design of nanowire structures because of various wetting states. Our findings demonstrate their potential applications in future deicing technology.

ASSOCIATED CONTENT

Supporting Information

This material is available free of charge via the Internet at http://pubs.acs.org.

AUTHOR INFORMATION

Corresponding Authors

*E-mail: jiangcy@nwpu.edu.cn. Tel: 86-29-88495102.
*E-mail: yuanwz@nwpu.edu.cn.

Notes

The authors declare no competing financial interest.

ACKNOWLEDGMENTS

The authors are thankful for the support from National Natural Science Foundation of China (Grant 51005187, 51375398), Fundamental Research Funds for the Central Universities (Grant 3102014JCS05001), 111 Project (Grant B13044), and Ao Xiang Star program of NPU.

REFERENCES

(1) Jung, S.; Tiwari, M. K.; Doan, N. V.; Poulikakos, D. Mechanism of Supercooled Droplet Freezing on Surfaces. *Nat. Commun.* **2012**, *3*, 615.
(2) Yao, X.; Song, Y.; Jiang, L. Applications of Bio-Inspired Special Wettable Surfaces. *Adv. Mater.* **2011**, *23*, 719−734.
(3) Cao, L.; Jones, A. K.; Sikka, V. K.; Wu, J.; Gao, D. Anti-Icing Superhydrophobic Coatings. *Langmuir* **2009**, *25*, 12444−12448.
(4) Tourkine, P.; Le Merrer, M.; Quéré, D. Delayed Freezing on Water Repellent Materials. *Langmuir* **2009**, *25*, 7214−7216.
(5) Jafari, R.; Menini, R.; Farzaneh, M. Superhydrophobic and Icephobic Surfaces Prepared by Rf-Sputtered Polytetrafluoroethylene Coatings. *Appl. Surf. Sci.* **2010**, *257*, 1540−1543.
(6) Kulinich, S.; Farhadi, S.; Nose, K.; Du, X. Superhydrophobic Surfaces: Are They Really Ice-Repellent? *Langmuir.* **2010**, *27*, 25−29.
(7) Jung, S.; Dorrestijn, M.; Raps, D.; Das, A.; Megaridis, C. M.; Poulikakos, D. Are Superhydrophobic Surfaces Best for Icephobicity? *Langmuir* **2011**, *27*, 3059−3066.
(8) Menini, R.; Farzaneh, M. Advanced Icephobic Coatings. *J. Adhes. Sci. Technol.* **2011**, *25*, 971−992.
(9) Farhadi, S.; Farzaneh, M.; Kulinich, S. Anti-Icing Performance of Superhydrophobic Surfaces. *Appl. Surf. Sci.* **2011**, *257*, 6264−6269.
(10) Li, J.; Zhao, Y.; Hu, J.; Shu, L.; Shi, X. Anti-Icing Performance of a Superhydrophobic Pdms/Modified Nano-Silica Hybrid Coating for Insulators. *J. Adhes. Sci. Technol.* **2012**, *26*, 665−679.
(11) Wang, H.; He, G.; Tian, Q. Effects of Nano-Fluorocarbon Coating on Icing. *Appl. Surf. Sci.* **2012**, *258*, 7219−7224.
(12) Nosonovsky, M.; Hejazi, V. Why Superhydrophobic Surfaces Are Not Always Icephobic. *ACS Nano* **2012**, *6*, 8488−8491.
(13) Arianpour, F.; Farzaneh, M.; Kulinich, S. Hydrophobic and Ice-Retarding Properties of Doped Silicone Rubber Coatings. *Appl. Surf. Sci.* **2013**, *265*, 546−552.

(14) Boinovich, L. B.; Emelyanenko, A. M.; Ivanov, V. K.; Pashinin, A. S. Durable Icephobic Coating for Stainless Steel. *ACS Appl. Mater. Interfaces* **2013**, *5*, 2549−2554.
(15) Chen, J.; Dou, R.; Cui, D.; Zhang, Q.; Zhang, Y.; Xu, F.; Zhou, X.; Wang, J.; Song, Y.; Jiang, L. Robust Prototypical Anti-Icing Coatings with a Self-Lubricating Liquid Water Layer between Ice and Substrate. *ACS Appl. Mater. Interfaces* **2013**, *5*, 4026−4030.
(16) Ruan, M.; Li, W.; Wang, B.; Deng, B.; Ma, F.; Yu, Z. Preparation and Anti-Icing Behavior of Superhydrophobic Surfaces on Aluminum Alloy Substrates. *Langmuir* **2013**, *29*, 8482−8491.
(17) Wang, Y.; Xue, J.; Wang, Q.; Chen, Q.; Ding, J. Verification of Icephobic/Anti-Icing Properties of a Superhydrophobic Surface. *ACS Appl. Mater. Interfaces* **2013**, *5*, 3370−3381.
(18) Zhang, Q.; He, M.; Chen, J.; Wang, J.; Song, Y.; Jiang, L. Anti-Icing Surfaces Based on Enhanced Self-Propelled Jumping of Condensed Water Microdroplets. *Chem. Commun.* **2013**, *49*, 4516−4518.
(19) Zhu, L.; Xue, J.; Wang, Y.; Chen, Q.; Ding, J.; Wang, Q. Ice-Phobic Coatings Based on Silicon-Oil-Infused Polydimethylsiloxane. *ACS Appl. Mater. Interfaces* **2013**, *5*, 4053−4062.
(20) Zhu, L.; Xue, J.; Wang, Y. Y.; Chen, Q. M.; Ding, J. F.; Wang, Q. J. Ice-Phobic Coatings Based on Silicon-Oil-Infused Polydimethylsiloxane. *ACS Appl. Mater. Interfaces* **2013**, *5*, 4053−4062.
(21) Chernyy, S.; Jarn, M.; Shimizu, K.; Swerin, A.; Pedersen, S. U.; Daasbjerg, K.; Makkonen, L.; Claesson, P.; Iruthayaraj, J. Superhydrophilic Polyelectrolyte Brush Layers with Imparted Anti-Icing Properties: Effect of Counter Ions. *ACS Appl. Mater. Interfaces* **2014**, *6*, 6487−6496.
(22) Dou, R. M.; Chen, J.; Zhang, Y. F.; Wang, X. P.; Cui, D. P.; Song, Y. L.; Jiang, L.; Wang, J. J. Anti-Icing Coating with an Aqueous Lubricating Layer. *ACS Appl. Mater. Interfaces* **2014**, *6*, 6998−7003.
(23) Petrenko, V.; Peng, S. Reduction of Ice Adhesion to Metal by Using Self-Assembling Monolayers (Sams). *Can. J. Phys.* **2003**, *81*, 387−393.
(24) Matsumoto, K.; Kobayashi, T. Fundamental Study on Adhesion of Ice to Cooling Solid Surface. *Int. J. Refrig.* **2007**, *30*, 851−860.
(25) Sarkar, D.; Farzaneh, M. Superhydrophobic Coatings with Reduced Ice Adhesion. *J. Adhes. Sci. Technol.* **2009**, *23*, 1215−1237.
(26) Davis, A.; Yeong, Y. H.; Steele, A.; Bayer, I. S.; Loth, E. Superhydrophobic Nanocomposite Surface Topography and Ice Adhesion. *ACS Appl. Mater. Interfaces* **2014**, *6*, 9272−9279.
(27) Dotan, A.; Dodiuk, H.; Laforte, C.; Kenig, S. The Relationship between Water Wetting and Ice Adhesion. *J. Adhes. Sci. Technol.* **2009**, *23*, 1907−1915.
(28) Kulinich, S.; Farzaneh, M. Ice Adhesion on Super-Hydrophobic Surfaces. *Appl. Surf. Sci.* **2009**, *255*, 8153−8157.
(29) Kulinich, S.; Farzaneh, M. How Wetting Hysteresis Influences Ice Adhesion Strength on Superhydrophobic Surfaces. *Langmuir* **2009**, *25*, 8854−8856.
(30) Meuler, A. J.; Smith, J. D.; Varanasi, K. K.; Mabry, J. M.; McKinley, G. H.; Cohen, R. E. Relationships between Water Wettability and Ice Adhesion. *ACS Appl. Mater. Interfaces.* **2010**, *2*, 3100−3110.
(31) Meuler, A. J.; McKinley, G. H.; Cohen, R. E. Exploiting Topographical Texture to Impart Icephobicity. *ACS Nano* **2010**, *4*, 7048−7052.
(32) Hassan, M.; Lee, H.; Lim, S. The Variation of Ice Adhesion Strength with Substrate Surface Roughness. *Meas. Sci. Technol.* **2010**, *21*, 075701.
(33) Zou, M.; Beckford, S.; Wei, R.; Ellis, C.; Hatton, G.; Miller, M. Effects of Surface Roughness and Energy on Ice Adhesion Strength. *Appl. Surf. Sci.* **2011**, *257*, 3786−3792.
(34) Guo, P.; Zheng, Y.; Wen, M.; Song, C.; Lin, Y.; Jiang, L. Icephobic/Anti-Icing Properties of Micro/Nanostructured Surfaces. *Adv. Mater.* **2012**, *24*, 2642−2648.
(35) Wang, L.; Wen, M. X.; Zhang, M. Q.; Jiang, L.; Zheng, Y. M. Ice-Phobic Gummed Tape with Nano-Cones on Microspheres. *J. Mater. Chem. A* **2014**, *2*, 3312−3316.
(36) He, Y.; Jiang, C.; Cao, X.; Chen, J.; Tian, W.; Yuan, W. Reducing Ice Adhesion by Hierarchical Micro-Nano-Pillars. *Appl. Surf. Sci.* **2014**, *305*, 589−595.
(37) He, Y.; Jiang, C.; Yin, H.; Chen, J.; Yuan, W. Superhydrophobic Silicon Surfaces with Micro−Nano Hierarchical Structures Via Deep Reactive Ion Etching and Galvanic Etching. *J. Colloid Interface Sci.* **2011**, *364*, 219−229.
(38) de Gennes, P. G., Brochard-Wyart, F., Quéré, D. *Capillarity and Wetting Phenomena*; Springer, Berlin, 2003.
(39) Bico, J.; Thiele, U.; Quere, D. Wetting of Textured Surfaces. *Colloid Surf., A* **2002**, *206*, 41−46.
(40) Marmur, A. A Guide to the Equilibrium Contact Angles Maze. In *Contact Angle, Wettability and Adhesion*; Mittal, K. L., Ed.; Brill: Leiden, The Netherlands, 2009; Vol. *6*, pp 3−18.
(41) Ishino, C.; Okumura, K.; Quere, D. Wetting Transitions on Rough Surfaces. *Europhys. Lett.* **2004**, *68*, 419−425.
(42) Patankar, N. A. Transition between Superhydrophobic States on Rough Surfaces. *Langmuir* **2004**, *20*, 7097−7102.
(43) Barbieri, L.; Wagner, E.; Hoffmann, P. Water Wetting Transition Parameters of Perfluorinated Substrates with Periodically Distributed Flat-Top Microscale Obstacles. *Langmuir* **2007**, *23*, 1723−1734.
(44) Cassie, A. B. D.; Baxter, S. Wettability of Porous Surfaces. *Trans. Faraday Soc.* **1944**, *40*, 0546−0550.
(45) Whyman, G.; Bormashenko, E. How to Make the Cassie Wetting State Stable? *Langmuir.* **2011**, *27*, 8171−8176.
(46) Whyman, G.; Bormashenko, E. Wetting Transitions on Rough Substrates: General Considerations. *J. Adhes. Sci. Technol.* **2012**, *26*, 207−220.
(47) Bormashenko, E.; Bormashenko, Y.; Whyman, G.; Pogreb, R.; Stanevsky, O. Micrometrically Scaled Textured Metallic Hydrophobic Interfaces Validate the Cassie-Baxter Wetting Hypothesis. *J. Colloid Interface Sci.* **2006**, *302*, 308−311.
(48) Bormashenko, E. Wetting of Real Solid Surfaces: New Glance on Well-Known Problems. *Colloid Polym. Sci.* **2013**, *291*, 339−342.
(49) Petrovic, J. Review Mechanical Properties of Ice and Snow. *J. Mater. Sci.* **2003**, *38*, 1−6.
(50) Ryzhkin, I. A.; Petrenko, V. F. Physical Mechanisms Responsible for Ice Adhesion. *J. Phys. Chem. B* **1997**, *101*, 6267−6270.
(51) Ishino, C.; Okumura, K. Nucleation Scenarios for Wetting Transition on Textured Surfaces: The Effect of Contact Angle Hysteresis. *Europhys. Lett.* **2006**, *76*, 464−470.
(52) Bormashenko, E.; Pogreb, R.; Whyman, G.; Erlich, M. Cassie-Wenzel Wetting Transition in Vibrating Drops Deposited on Rough Surfaces: Is the Dynamic Cassie-Wenzel Wetting Transition a 2d or 1d Affair? *Langmuir* **2007**, *23*, 6501−6503.
(53) Bahadur, V.; Garimella, S. V. Preventing the Cassie-Wenzel Transition Using Surfaces with Noncommunicating Roughness Elements. *Langmuir* **2009**, *25*, 4815−4820.